ACS NANO

www.acsnano.org

ARTICLE

Spatially Uniform and Quantitative Surface-Enhanced Raman Scattering under Modal Ultrastrong Coupling Beyond Nanostructure Homogeneity Limits

Yoshiki Suganami, Tomoya Oshikiri, Hideyuki Mitomo, Keiji Sasaki, Yen-En Liu, Xu Shi, Yasutaka Matsuo, Kuniharu Ijiro, and Hiroaki Misawa*

Cite This: *ACS Nano* 2024, 18, 4993−5002

Read Online

ACCESS | Metrics & More | Article Recommendations | Supporting Information

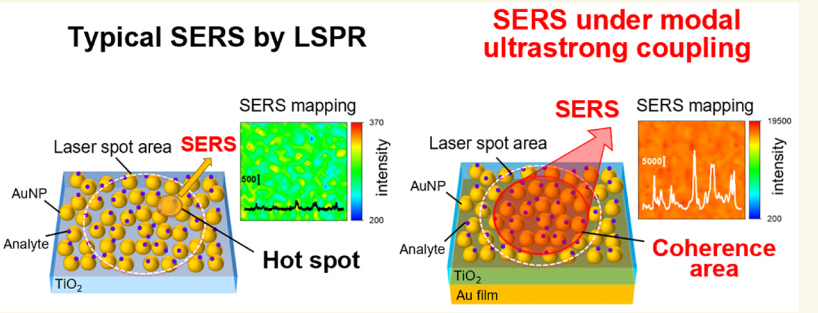

ABSTRACT: **We developed a substrate that enables highly sensitive and spatially uniform surface-enhanced Raman scattering (SERS). This substrate comprises densely packed gold nanoparticles (d-AuNPs)/titanium dioxide/Au film (d-ATA). The d-ATA substrate demonstrates modal ultrastrong coupling between localized surface plasmon resonances (LSPRs) of AuNPs and Fabry−Pérot nanocavities. d-ATA exhibits a significant enhancement of the near-field intensity, resulting in a 78-fold increase in the SERS signal for crystal violet (CV) compared to that of d-AuNP/TiO_2 substrates. Importantly, high sensitivity and a spatially uniform signal intensity can be obtained without precise control of the shape and arrangement of the nanoscale AuNPs, enabling quantitative SERS measurements. Additionally, SERS measurements of rhodamine 6G (R6G) on this substrate under ultralow adsorption conditions (0.6 R6G molecules/AuNP) show a spatial variation in the signal intensity within 3%. These findings suggest that the SERS signal under modal ultrastrong coupling originates from multiple plasmonic particles with quantum coherence.**

KEYWORDS: *localized surface plasmon resonance, modal ultrastrong coupling, surface-enhanced Raman scattering, quantum coherence, self-assembly*

INTRODUCTION

Surface-enhanced Raman scattering (SERS) is a sensing technique that allows label-free and sensitive detection of chemical and biological molecules on metal nanostructures.[1−5] The primary mechanism for enhancing Raman signals involves a significant electromagnetic enhancement due to local confinement of the electromagnetic field at so-called "hot spots" produced by localized surface plasmon resonances (LSPRs) of noble metals, such as silver or gold nanostructures. In particular, a narrower gap between these plasmonic nanostructures can generate a stronger electromagnetic field through the near-field coupling of LSPRs,[6−8] enabling ultrasensitive SERS measurements at the single-molecule level.[9−11] However, the surface nanostructure of a typical plasmonic substrate has spatial variability, leading to a random arrangement of hot spots on the substrate with a broad distribution of the electric field intensity.[12−14] The SERS signal

Received: November 6, 2023
Revised: January 24, 2024
Accepted: January 25, 2024
Published: February 1, 2024

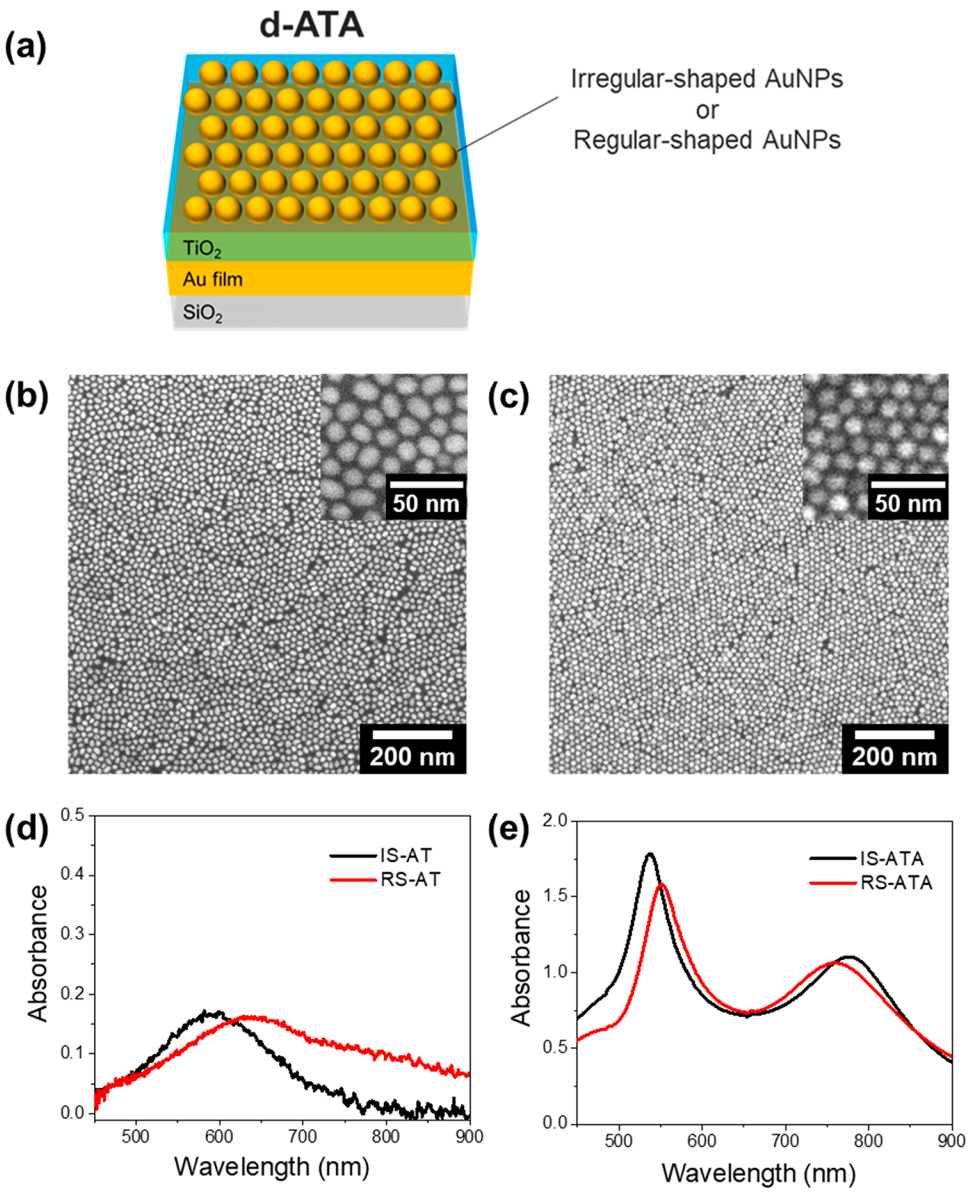

Figure 1. (a) Schematic of the d-ATA substrate. Top-view SEM images of (b) IS-ATA and (c) RS-ATA before ozone cleaning. The average sizes of these AuNPs were 15.4 and 14.3 nm, respectively. Absorption spectra of the (d) d-AT and (e) d-ATA structures.

intensity obtained from a typical plasmonic substrate is spatially nonuniform, which is a major reason for the poor quantitative results.

By utilizing a self-assembly method to fabricate a close-packed arrangement of metal nanoparticles, spatially nearly uniform and dense hot spots can be generated on the substrate.[15,16] This method has attracted much attention in recent years as a technique for realizing highly sensitive and uniform SERS measurements.[17−21] Achieving higher sensitivity with SERS requires spatially narrow nanoscale interparticle gaps that exhibit strong LSPR coupling.[22] At this scale, even small differences in the gap distance can cause large variations in the near-field intensity. Therefore, attaining both high sensitivity and spatial uniformity necessitates precise sub-nanoscale control over the arrangement of metallic nanoparticles. However, such control is difficult to achieve in practice.[23,24] The dilemma with using homogeneous structures for SERS measurements lies in the fact that minor deviations in the nanostructure can greatly compromise the quantitative nature of the measurement. Moreover, hot spots are located at narrow gaps between the metal nanoparticles. Because the hot spots locally exist only at narrow gaps between metal nanoparticles and analytes attach to various positions on gold nanoparticles (AuNPs), particularly under low adsorption conditions, the spatial variation in the Raman signal intensity becomes significant.[25,26] This limits the ability to obtain reproducible SERS signals through methodologies that improve nanostructure uniformity. Therefore, the development of SERS sensing substrates that simultaneously achieve both high sensitivity and spatial uniformity of the signal intensity for low concentrations of analytes in biological and chemical sensing remains a significant challenge.

We recently reported that SERS measurements on a substrate exhibiting modal coupling between Fabry−Pérot (FP) nanocavities and the LSPR of nonuniformly sized AuNPs fabricated through thermal melting improved both the intensity and spatial uniformity of the SERS signal compared to a substrate without FP nanocavities.[27] Finite difference time

https://doi.org/10.1021/acsnano.3c10959
ACS Nano 2024, 18, 4993−5002

domain (FDTD) simulations indicated that the enhancement in the SERS signal intensity due to modal coupling was a result of the near-field strength enhancement. Additionally, the spatial uniformity of the SERS signal intensity was attributed to coherent interactions induced between the LSPRs of AuNPs via FP nanocavities, leading to SERS signals originating from multiple AuNPs that are coherently interacting. We further confirmed the existence of quantum coherent interactions between the LSPRs of gold nanodisks (AuNDs) via FP nanocavities using a substrate with AuNDs fabricated on FP nanocavities, where both the AuND size and arrangement were precisely controlled using electron-beam lithography.[28] On the basis of these findings, we expected that the increase in the coupling strength improves the sensitivity and spatial uniformity of SERS signals rather than the conventional approaches based on the control of the geometric homogeneity of nanostructures. For an increase in the coupling strength, an increase in the number density of oscillators (nanoparticles) is a simple way. However, our previous approaches could not allow a further increase in the nanoparticle density.

In this study, we developed a nanostructure for which modal ultrastrong coupling is formed through densely packed AuNPs (d-AuNPs) on FP nanocavities using a self-assembly method. SERS measurements using this structure yielded a spatially uniform and intensely strong signal over a wide area. Importantly, SERS measurements of rhodamine 6G (R6G), which has very low adsorption on this substrate (0.6 to 24 molecules/AuNP), exhibited a spatial variation in the signal intensity of less than 3%. Additionally, extremely sensitive and quantitative SERS measurements were achieved, even without precise control of the shape or spatial arrangement of the AuNPs on a nanoscale. This enables quantitative measurements even at extremely low analyte adsorptions. These findings strongly suggest that, in SERS using plasmonic particles forming modal ultrastrong couplings with FP nanocavities, the SERS signals from the coherence area are coherent, and the SERS field amplitudes are averaged. This methodology represents an approach that simultaneously achieves the high sensitivity and spatial uniformity of the signal intensity in SERS.

RESULTS AND DISCUSSION

First, we fabricated d-AuNP/titanium dioxide (TiO_2)/Au film (d-ATA) structures and, as a control, d-AuNP/TiO_2 (d-AT) structures. To evaluate the influence of the gap distance distribution arising from the irregularity in the shape of AuNPs on the SERS homogeneity, these structures were fabricated with irregular spherical AuNPs (IS-AuNPs) prepared through a common citrate reduction method[29] and with commercially available regular spherical AuNPs (RS-AuNPs), referred to as IS-ATA, IS-AT, RS-ATA and RS-AT, respectively (Figure 1a). The absorption spectra of both IS-AuNP and RS-AuNP colloidal solutions showed an LSPR peak at 520 nm, and their spectral shapes were almost identical (Figure S1). Self-assembly techniques were employed to load d-AuNPs onto the TiO_2 of each structure.[16,30] These AuNPs were functionalized with 1-dodecanethiol (DDT) to allow for small interparticle gaps. DDT-modified AuNPs (AuNP@DDT) were dispersed in a chloroform solution. This AuNP@DDT solution was dropped onto the surface of Milli-Q water, providing a d-AuNP monolayer at the air−water interface. The d-AuNP monolayer was transferred onto the TiO_2 surface by the Langmuir−Schaefer method.[31] Scanning electron microscopy (SEM) images of IS-ATA and RS-ATA surfaces are shown in Figure 1b and c. Finally, the DDT coating of the surface was removed by an ozone cleaning process. SEM images of the IS-ATA and RS-ATA surfaces after ozone cleaning are shown in Figure S2a and b. After the ozone cleaning treatment, the spatial homogeneity of the d-AuNP arrangement in both IS-ATA and RS-ATA deteriorated (Figure S2a and b). The AuNP sizes for IS-ATA and RS-ATA after ozone cleaning were 15.4 ± 2.2 nm and 14.3 ± 1.2 nm, respectively, whereas the aspect ratios of the long and short diameters in IS-ATA and RS-ATA measured 1.29 ± 0.22 and 1.13 ± 0.09, respectively. These findings indicate a larger variation in the AuNP shape in IS-ATA. In addition, the surface coverages of AuNPs were 66.3% for IS-ATA and 66.7% for RS-ATA, confirming the high-density loading of AuNPs on TiO_2 of the FP nanocavities. To evaluate the structural homogeneity of IS-ATA and RS-ATA, we calculated the Voronoi areas for each AuNP. The coefficients of variation for these areas were 30% and 21% (Figure S2c and d), respectively. The results suggest that the d-AuNPs in IS-ATA exhibited a relatively wide gap distance distribution, whereas the d-AuNPs in RS-ATA were more spatially uniformly distributed even after ozone cleaning (Figure S2a−d).

Figure 1d and e show the absorption spectra of each substrate. Although there was no significant difference in the spectral shapes of IS-AuNPs and RS-AuNPs dispersed in solution (Figure S1), the absorption peak of RS-AT was red-shifted by 40 nm and exhibited broadening compared to IS-AT. This indicates that when AuNPs are densely loaded on the substrate by the self-assembly method, the gap distance between AuNPs becomes nonuniform due to variations in the shape of IS-AuNPs, resulting in differences in the absorption spectra. The absorption peaks for both IS-ATA and RS-ATA significantly split into two distinct peaks in the 500−900 nm range due to the formation of two new hybrid states.

Modal coupling is the state in which energy is exchanged between two modes via photons. As the rate of energy exchange by photons increases, the coupling strength increases and modal strong coupling is formed. In strong coupling between LSPR modes and nanocavity modes, two new hybrid modes are formed by hybridization between the modes. For modal strong coupling, the splitting energy between the hybrid modes must satisfy the condition shown in eq 1.

$$\hbar\Omega > \sqrt{\frac{\gamma_{UB}^{\ 2}}{2} + \frac{\gamma_{LB}^{\ 2}}{2}} = \sqrt{\frac{\gamma_{cavity}^{\ 2}}{2} + \frac{\gamma_{LSPR}^{\ 2}}{2}} \quad (1)$$

where $\hbar\Omega$ is the splitting energy, γ_{UB} and γ_{LB} are the line widths of the upper and lower branch modes, and γ_{cavity} and γ_{LSPR} are the line widths of the FP nanocavity and LSPR modes, respectively.[32] Furthermore, when the energy of the noninteracting states of the LSPR and nanocavity modes is $\hbar\omega_0$, the modal coupling states with splitting energies $\hbar\Omega > 0.2\hbar\omega_0$ are defined as ultrastrong coupling conditions.[33] In Figure S3, dispersion curves were prepared by plotting the peak energies of the upper and lower branch modes as functions of the wavenumber of the lowest-order FP nanocavity modes in d-ATA with different TiO_2 film thicknesses to tune the condition between the LSPR and FP nanocavity modes. It was confirmed that the almost zero detuning conditions were achieved when the TiO_2 film thicknesses were 31 and 33 nm for IS-ATA and RS-ATA,

https://doi.org/10.1021/acsnano.3c10959
ACS Nano 2024, 18, 4993−5002

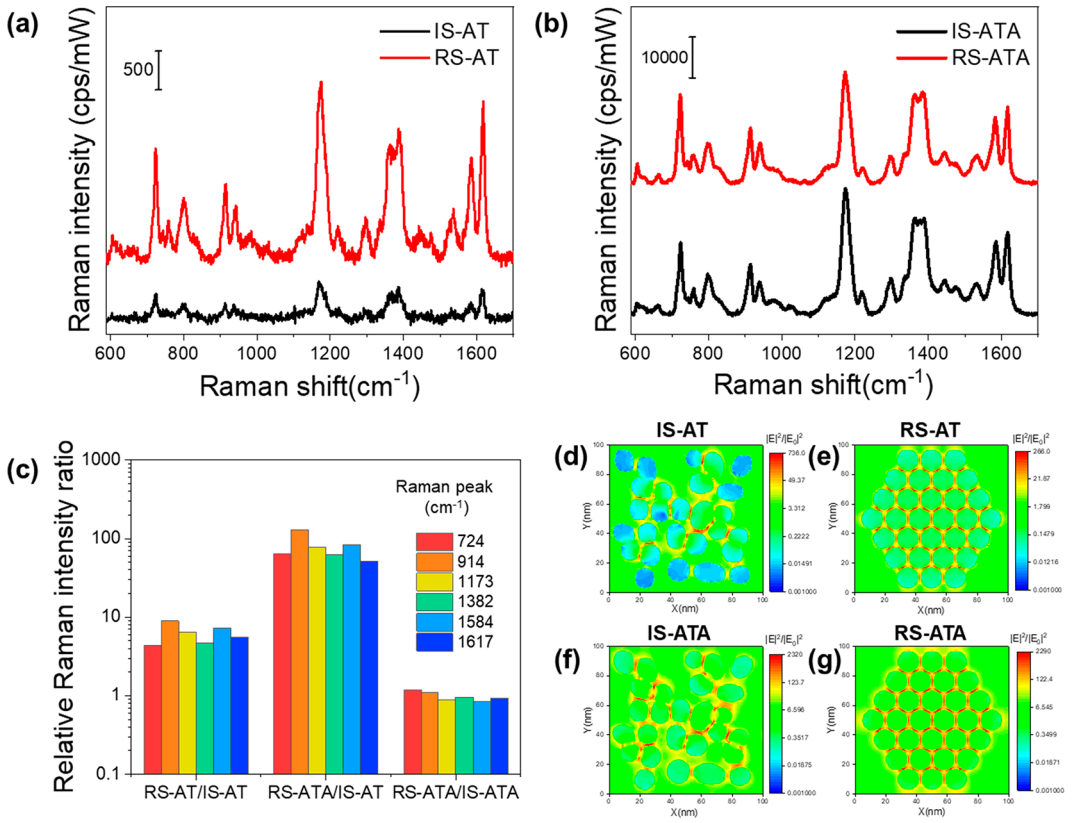

Figure 2. (a, b) Raman spectra of CV (1 μM) on each substrate obtained by using 785 nm laser excitation. The laser power was 50 μW. (c) Relative Raman intensity ratios for different Raman peaks obtained from (a) and (b). (d–g) Cross-sectional near-field distributions at 785 nm. The model for IS-AuNPs was based on the SEM image in Figure S2a, whereas the model for RS-AuNPs was an ideal uniform spatial arrangement model to understand the effects of heterogeneity in the AuNP sequence.

respectively. The splitting energies for IS-ATA and RS-ATA calculated from the harmonic oscillator model[32] were $0.34\hbar\omega_0$ (680 meV) and $0.35\hbar\omega_0$ (670 meV), respectively (Figure S3). These results confirm the formation of ultrastrong coupling in both structures.

In modal ultrastrong coupling, the LSPRs of multiple AuNPs quantum coherently interact via a nanocavity. The authors report that in modal strong coupling, the range of quantum coherent interaction (coherence area) is estimated to be a circle with a diameter of approximately 500 nm.[28] The dephasing time of the LSPR under this modal strong coupling condition is less than 10 fs, defining the size of the coherence area. Therefore, modal ultrastrong coupling is considered to have a coherence area almost the same as that of modal strong coupling. The SERS from modal strong coupling or ultrastrong coupling within such a coherence area is coherent. In other words, the field amplitudes of SERS from gold nanostructures within the coherence area are averaged.

Let us now consider the SERS intensity integrated over the region S. The intensity is expressed by the following equation:

$$I = \frac{1}{S}\int_S I(\boldsymbol{r})\,\mathrm{d}\boldsymbol{r} \tag{2}$$

where $I(\boldsymbol{r})$ is the intensity distribution as a function of spatial coordinate $\boldsymbol{r}$. The variance in the integrated intensity is statistically given by

$$\begin{aligned}\sigma^2 &= \langle (I - \langle I\rangle)^2\rangle \\ &= \frac{1}{S^2}\iint_S \langle (I(\boldsymbol{r}_1) - \langle I\rangle)(I(\boldsymbol{r}_2) - \langle I\rangle)\rangle\,\mathrm{d}\boldsymbol{r}_1\,\mathrm{d}\boldsymbol{r}_2 \\ &= \frac{1}{S^2}\iint_S [\langle I(\boldsymbol{r}_1)I(\boldsymbol{r}_2)\rangle - \langle I\rangle^2]\,\mathrm{d}\boldsymbol{r}_1\,\mathrm{d}\boldsymbol{r}_2\end{aligned} \tag{3}$$

where $\langle\bullet\rangle$ represents the ensemble average. This equation can be rewritten as

$$\sigma^2 = \frac{1}{S^2}\iint_S \{g^{(2)}(\boldsymbol{r}_1, \boldsymbol{r}_2) - 1\}\langle I\rangle^2\,\mathrm{d}\boldsymbol{r}_1\,\mathrm{d}\boldsymbol{r}_2 \tag{4}$$

Here, the second-order coherence function $g^{(2)}(\boldsymbol{r}_1,\boldsymbol{r}_2)$ is defined as

$$g^{(2)}(\boldsymbol{r}_1, \boldsymbol{r}_2) = \frac{\langle I(\boldsymbol{r}_1)I(\boldsymbol{r}_2)\rangle}{\langle I(\boldsymbol{r}_1)\rangle\langle I(\boldsymbol{r}_2)\rangle} \tag{5}$$

When the electric fields at two positions $\boldsymbol{r}_1$ and $\boldsymbol{r}_2$ are perfectly coherent (perfectly correlated), $g^{(2)}(\boldsymbol{r}_1,\boldsymbol{r}_2) = 1$, which is the minimum value of $g^{(2)}$. In contrast, in the case of spatial incoherence (uncorrelated) between positions $\boldsymbol{r}_1$ and $\boldsymbol{r}_2$, $1 \le g^{(2)}(\boldsymbol{r}_1,\boldsymbol{r}_2) \le \infty$, depending on the randomness of the intensity distribution $I(\boldsymbol{r})$. Comparing the second-order coherence functions of the d-AT structure with inhomogeneously distributed hot spots, $g^{(2)}_{d\text{-}AT}(\boldsymbol{r}_1,\boldsymbol{r}_2)$, and d-ATA with a quantum coherence area, $g^{(2)}_{d\text{-}ATA}(\boldsymbol{r}_1,\boldsymbol{r}_2)$,

$$g^{(2)}_{d\text{-}AT} \ge g^{(2)}_{d\text{-}ATA} \approx 1 \text{ at any } (\boldsymbol{r}_1, \boldsymbol{r}_2) \tag{6}$$

https://doi.org/10.1021/acsnano.3c10959
ACS Nano 2024, 18, 4993–5002

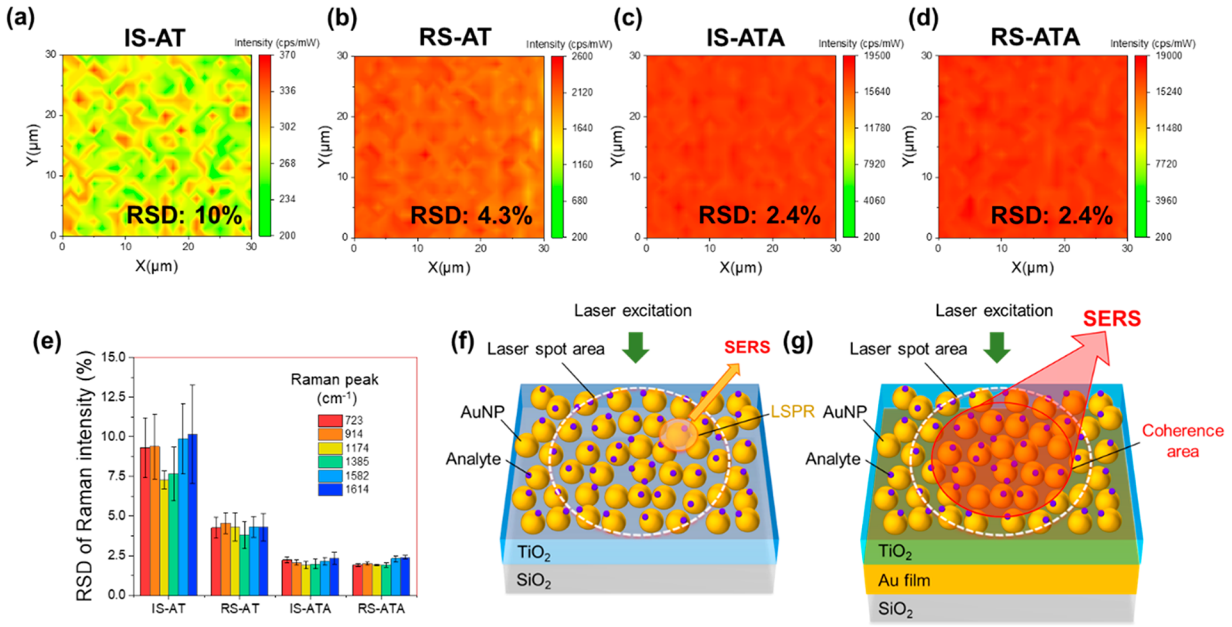

Figure 3. Raman mapping images of CV (1 μM) on (a) IS-AT, (b) RS-AT, (c) IS-ATA, and (d) RS-ATA substrates around a wavenumber of 1617 cm^{-1} obtained by using 785 nm laser excitation. The laser power was 0.5 mW. (e) RSDs of Raman intensities at different Raman peaks obtained from Raman mapping of CV (1 μM). Schematic illustrations of SERS excitation under (f) LSPR and (g) modal ultrastrong coupling. The red area indicates the coherence area, and SERS would be emitted from all analyte molecules within the coherence areas.

Therefore, the variance in the SERS intensity from the d-ATA structure can be expected to be drastically smaller than that from the d-AT structure.

The SERS intensity on each substrate was evaluated using a crystal violet (CV) as the analyte. The substrates were immersed in 5 mL of an aqueous solution of CV (1 μM) for 1 h, rinsed with Milli-Q water, and air-dried. While typical Raman experiments use lasers with excitation wavelengths of either 532 or 785 nm, a 785 nm laser was opted for in this study. This choice was made to avoid potential complications in the analysis of SERS properties caused by the d-band to sp-band transition absorption of gold.[34] Figure 2a shows the SERS spectra of IS-AT and RS-AT. Raman peaks attributed to CV were observed for both IS-AT and RS-AT. The assignments of Raman bands of CV are provided in Table S1 of the Supporting Information. The average Raman intensity calculated from 6 peaks (at 724, 914, 1173, 1382, 1584, and 1617 cm^{-1}) of RS-AT was 6 times (6 ± 1.7) higher than that of IS-AT (Figure 2c). This difference can be attributed to the evenly spaced gaps between AuNPs in RS-AT, where CV molecules are adsorbed at hot spots between AuNPs. The relatively high optical absorption of RS-AT at 785 nm (Figure 1d) suggests that the coupling mode between LSPRs affects the SERS intensity enhancement.

An electromagnetic field analysis was performed by using FDTD simulations to gain insight into the SERS enhancement. For the simulation model in this analysis, a periodic structure with uniformly spaced AuNPs was assumed (Figure S4a). No significant difference in the near-field strength between IS-AT and RS-AT was found with this model (Figure S4c). Then, FDTD simulations using two models with different distributions of the gap distances between AuNPs (Figures 2d and e and S5) were performed. The model for IS-AuNPs was based on the SEM image in Figure S2a, whereas the model for RS-AuNPs was based on an ideal uniform spatial arrangement model to understand the effects of AuNP sequence heterogeneity. The maximum near-field intensity for IS-AT was 2.8 times higher than that for RS-AT. However, the near-field intensity for IS-AT showed a greater coefficient of variation (431%) than that for RS-AT (353%), highlighting that the uniformity of the AuNP sequence significantly impacts the SERS intensity in LSPR-based AT structures.

Next, we compared the SERS spectra of IS-ATA and RS-ATA. Surprisingly, the average Raman intensities of the two were nearly identical and approximately 80 times (78 ± 27) higher than those of IS-AT (Figure 2b and c). The peak intensity ratio variation depended on the IS-AT peak intensity. From the near-field spectra in Figure S4c, the near-field intensity for RS-ATA at 785 nm was approximately 10 times higher than that for RS-AT. Moreover, IS-ATA and RS-ATA showed almost the same maximum near-field intensities (Figure 2f and g). These findings suggest that the spatial arrangement of AuNPs in d-ATA has a minor impact because the electric field enhancement resulting from the coupling between the nanocavity modes and LSPRs significantly outweighs that from the coupling between LSPRs. Additionally, the longitudinal (z-axis) cross-sectional near-field distributions (Figure S6) support the total enhancement of the electric field intensities via the modal ultrastrong coupling.

To examine the effect of modal ultrastrong coupling on the spatial homogeneity of the SERS intensity, Raman mapping was conducted on a 30 × 30 μm^2 area (625 measurements) of CV molecules (1 μM) adsorbed on each substrate. The objective lens magnification was 50× (0.75 NA). The spatial homogeneity was evaluated by calculating the relative standard deviation (RSD), which is the standard deviation of the Raman intensity divided by the mean intensity. Figure 3a–d shows Raman mapping images at 1617 cm^{-1}. The RSDs of IS-AT and RS-AT were 10% and 4.3%, respectively. This result is attributed to the spatial distribution of AuNPs. Conversely, the RSDs of IS-ATA and RS-ATA were even lower (2.4%), resulting in highly spatially homogeneous Raman mapping

https://doi.org/10.1021/acsnano.3c10959
ACS Nano 2024, 18, 4993−5002

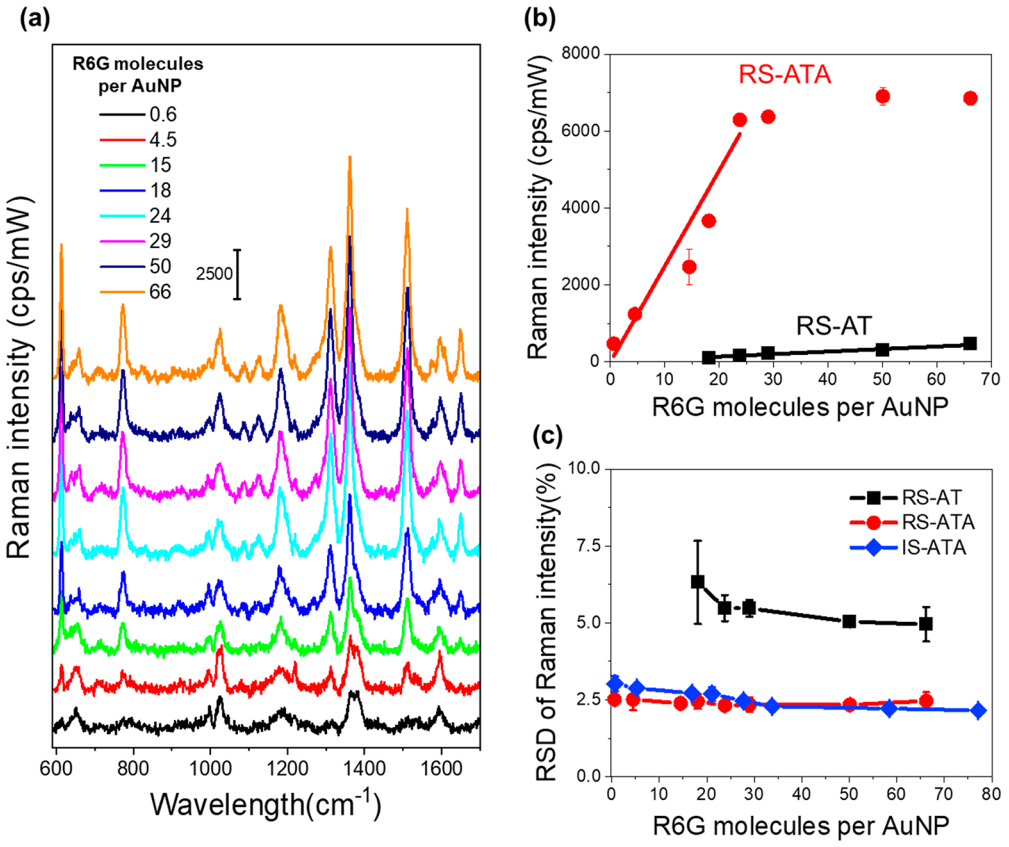

Figure 4. (a) Raman spectra for different numbers of adsorbed R6G molecules per AuNP on RS-ATA. The laser power was 0.5 mW. The number of adsorbed R6G molecules varied from 0.6 to 66 molecules/AuNP. (b) Characteristic Raman signal intensities of RS-ATA (red) and RS-AT (black) around a wavenumber of 614 cm^{-1} as a function of the number of R6G molecules per AuNP on d-AuNPs. The red and black lines represent the linear regression to RS-ATA and RS-AT, respectively. RS-ATA was curve fitted in the range below 24 R6G molecules/AuNP. The correlation coefficients *R* of these lines are 0.991 for RS-ATA and 0.997 for RS-AT. (c) RSD of the Raman signal intensity of RS-AT (black), RS-ATA (red), and IS-ATA (blue) around a wavenumber of 614 cm^{-1} as a function of the number of R6G molecules on AuNPs. RS-AT could not be measured due to insufficient signal intensity in the 0.6−15 R6G molecules/AuNP range. The error bars of the graph were obtained from three experiments.

images. Moreover, the RSDs of both d-ATA substrates at six Raman peaks in the range of 700−1700 cm^{-1} were all below 2.5% (Figure 3e), demonstrating highly homogeneous Raman measurements regardless of the Raman shift. These results can be understood by the quantum coherence in modal ultrastrong coupling. Figure 3f and g schematically illustrate the mechanism of this scenario. When light is incident on the AuNPs without an FP nanocavity (Figure 3f), the incident light randomly couples with the LSPRs of individual AuNPs, and SERS is excited from molecules adsorbed at each hot spot. Thus, IS-AT with a large spatial variation produces a nonuniform Raman signal. In d-ATA, AuNPs within the coherence area share an incident light field through the FP nanocavity (Figure 3g). Raman scattering is generated from all molecules adsorbed throughout the coherence area, and the SERS amplitudes within the coherence area are averaged. As a result, many AuNPs can share a Raman scattering field under modal ultrastrong coupling with the d-AuNPs in the coherence area, and the heterogeneity of the d-AuNP array becomes ignorable. This allows for spatially highly homogeneous Raman measurements. Furthermore, the FDTD simulation showed that the coefficient of variation of the near-field intensity for IS-ATA was 361%, which was higher than that for RS-ATA (354%) in Figure 2f and g, indicating a difference in their spatial near-field strength. Nevertheless, the lack of difference in the spatial homogeneity of the SERS intensity for both structures supports the quantum coherence effect on the uniformity of the SERS signal.

We further investigated the effect of nonuniformity in the arrangement of d-AuNPs on the homogeneity of SERS by performing Raman mapping over a larger area of 1 × 1 mm^2 (Figure S7). The objective lens magnification was 5× (0.12 NA). The laser power was 4.6 mW. The RSDs of both IS-AT (18%) and RS-AT (7.8%) deteriorated compared to the results of 30 × 30 μm^2 area Raman mapping in Figure 3b. In contrast, Raman mapping for RS-ATA and IS-ATA still showed low RSDs of approximately 4% or less. The laser spot areas for Raman mapping of 30 × 30 μm^2 and 1 × 1 mm^2 were calculated as 1.28 μm^2 and 50 μm^2, respectively. These values are based on the laser spot diameter and objective lens, as described in the Methods section. In our previous study, we calculated the coherence area to be approximately 500 nm in diameter from the splitting energy calculation.[28] We assume that the Raman signal for d-ATA is averaged over a coherence area of an equivalent size. The RSDs of the Raman mappings at the two different scales are nearly identical. This observation confirms that the presence of a coherence area as large as 500 nm can provide a spatially uniform Raman signal intensity regardless of the laser spot area.

https://doi.org/10.1021/acsnano.3c10959
ACS Nano 2024, 18, 4993−5002

Finally, quantitative SERS measurements and Raman mapping, depending on the number of molecules adsorbed on d-AuNPs, were conducted. The fluorescent molecule R6G was employed to evaluate the quantity of molecules adsorbed on each AuNP. The adsorption of R6G molecules on each AuNP was controlled by varying the contact time of a 1 μM R6G aqueous solution with the substrate surface. The number of adsorbed R6G/AuNPs was calculated by measuring the fluorescence intensity of the collected R6G solution (Figure S8). The absorption spectra are shown in Figure S9. From the spectra of R6G-decorated IS-AT, the absorption peak slightly red-shifted from approximately 600 to 605 nm as the adsorption of R6G increased. This absorption band shift could be attributed to the coupling between LSPRs and transition dipoles of the R6G molecules.[35] In the case of RS-AT, Raman peaks were observed for 18 R6G molecules per AuNP (Figure S10), whereas for RS-ATA, Raman peaks were observed even under low R6G adsorption conditions of 0.6 molecules per AuNP (Figure 4a). No Raman peaks were observed for IS-AT under any R6G adsorption condition. Figure 4b shows the Raman intensity at 614 cm^{-1} depending on the number of adsorbed R6G molecules. RS-ATA showed a linear response (correlation coefficient $R > 0.99$) in the range of 0.6−24 R6G molecules per AuNP, confirming the feasibility of quantitative Raman measurements. Moreover, Raman mappings of a 30 × 30 μm^2 area were conducted under different numbers of adsorbed R6G molecules (Figures S11−S13). The RSD is shown in Figure 4c. Both IS-ATA and RS-ATA exhibited RSDs of less than 3% across all R6G molecule adsorption conditions, indicating a more spatially uniform Raman intensity compared to RS-AT (RSD < 6.3%). The RSD of RS-AT increased as the number of adsorbed R6G molecules per AuNP decreased (5.0−6.3%). Measurements below 20 molecules per AuNP were unfeasible due to detection sensitivity limitations. The RSD is anticipated to further increase with fewer adsorbed molecules per AuNP due to significant variations in the adsorption sites. In contrast, RS-ATA maintained relatively low RSDs regardless of the number of adsorbed R6G molecules (2.3−2.5%). Under the condition of 0.6 R6G molecules per AuNP, approximately 3,200 molecules (5.3×10^{-21} M) were adsorbed on the laser spot area of the substrate containing 5,300 AuNPs. Despite the potential for large variations in the adsorption positions of R6G molecules on d-AuNPs, spatially homogeneous Raman intensities were obtained. This observation supports the interpretation that SERS originates from the entire coherence area due to quantum coherence in modal ultrastrong coupling. These results demonstrate that d-ATA substrates enable highly sensitive, spatially homogeneous, and quantitative Raman measurements even under low analyte adsorption conditions.

CONCLUSIONS

Quantitative SERS measurements using a SERS substrate with LSPR under low molecule adsorption conditions are generally difficult due to the nonuniformity of the SERS signal intensity. To address this issue, we developed a structure composed of d-AuNPs on FP nanocavities that exhibits modal ultrastrong coupling by using a self-assembly method. SERS measurements using this structure yielded strong and spatially uniform signals over a wide area. High-sensitivity and quantitative SERS measurements were achieved without the need for precise control over the nanoscale shape or arrangement of the d-AuNPs. Furthermore, even in SERS measurements using R6G, which showed very low and limited adsorption on this substrate (0.6 to 24 molecules per AuNP), the spatial variation in the signal intensity remained within 3%. This enabled quantitative measurements even at extremely low analyte adsorptions. These findings strongly suggest that in SERS utilizing plasmonic particles forming modal ultrastrong coupling with FP nanocavities, the signal arises from multiple plasmonic particles with quantum coherent interactions within the coherence area. Although the detection range for quantitative analysis on RS-ATA is limited at low adsorption levels due to their signal saturation, d-ATA devices can become practical SERS substrates by overcoming this issue. Overall, we have established a methodology that enables both high SERS sensitivity and reproducibility, which have a trade-off relation for conventional LSPR-based SERS substrates.

METHODS

Materials. Fifteen nanometer AuNPs (RS-AuNPs) were purchased from BBI Solutions. Crystal violet (CV), 1-dodecanethiol (DDT), chloroform, trisodium citrate, acetic acid, and tannic acid were purchased from Wako Pure Chemical Industries, Ltd. Rhodamine 6G (R6G) and propylphosphoric acid were purchased from Tokyo Chemical Industry (TCI) Co., Ltd.

Synthesis of IS-AuNPs. A water solution of IS-AuNPs was synthesized by mixing 20 mL of trisodium citrate (0.2% w/v) and 16 μL of tannic acid (1% w/v) with 294 μL of $HAuCl_4$ (0.1 M) in 80 mL of Milli-Q, boiling it in the oil bath at 120 °C, and maintaining it for 10 min.

Surface Modification of AuNPs. DDT-modified RS (or IS)-AuNPs (AuNPs@DDT) were prepared by using a two-step ligand exchange method. In this step, DDT (350 μL) with a chloroform solution (6.65 mL) was transferred to 20 mL of an RS-AuNP (2.32 nM) solution with acetic acid (340 μL) and vigorously stirred for 30 s. The mixture was then ultrasonicated for 30 min. Then, the top water solution was removed. Finally, a centrifuge was utilized to purge the AuNPs@DDT/chloroform solution.

Fabrication of d-AuNP/TiO_2/Au-Film (d-ATA) Substrates. The d-ATA structure with RS-AuNPs (RS-ATA) or IS-AuNPs (IS-ATA) was fabricated on a silica glass substrate. First, Fabry−Pérot (FP) nanocavities (TiO_2/Au film) were constructed. The silica substrates were cleaned with acetone, methanol, and deionized water in an ultrasonic bath for 3 min and dried with airflow. A 3 nm titanium film, a 100 nm Au film, and a 0.5 nm titanium film were sequentially sputtered on the surface of silica glass by using a helicon sputter (ULVAC, MPS-4000C1/HC1). A 31 or 33 nm TiO_2 film was deposited by an atomic layer deposition (ALD) system (SUNALE R series, Picosun) on the Au film at 300 °C with titanium tetrachloride ($TiCl_4$) and H_2O as precursors. The substrate was submerged in propylphosphoric acid in an ethanol solution (2 mM) for 12 h to hydrophobize the TiO_2 surface. A d-AuNP monolayer was formed by dropping a chloroform solution of AuNPs@DDT onto the Milli-Q water surface. Subsequently, the d-AuNP monolayer was transferred to the TiO_2 surface of the FP nanocavities. Finally, an ozone cleaning process was performed in a commercial UV/ozone cleaner (UV-1, SAMCO) for 2 h at 40 °C to remove DDT molecules on d-ATA. This cleaner contained a low-pressure mercury vapor lamp that could irradiate 110 W ultraviolet light at wavelengths of 254 nm (~85%) and 185 nm (~15%). This cleaning process was performed without direct UV irradiation for the sample.

Sample Characterization. The absorption spectra of the AuNP colloidal solutions were measured by a UV−vis spectrophotometer (Shimadzu UV3100PC). The reflection spectra of d-ATA were measured with a spectroscopic reflectometer (F20-UV, Filmetrics). The reflection and transmission spectra of d-AT were measured by a photonic multichannel analyzer (Hamamatsu Photonics, PMA C7473) equipped with an optical microscope (Olympus, BX-51). The absorption spectra of d-AT and d-ATA were calculated as $-\log(T + R)$ and $-\log(R)$ as functions of wavelength, respectively, using

https://doi.org/10.1021/acsnano.3c10959
ACS Nano 2024, 18, 4993−5002

the reflection R and the transmission T. The transmission of d-ATA was zero due to the presence of a gold reflective film. The surface morphology was observed by field-emission scanning electron microscopy (SEM, SU8230, Hitachi High-Technologies Corporation) with a maximum resolution of 1 nm at an electron accelerating voltage of 10 kV.

Raman Measurements. A Raman microscope system (Renishaw, inVia Reflex) with a 50× objective lens (0.75 NA, Leica) in a certain configuration was used for SERS measurements. A 785 nm laser was used as the excitation source. The laser spot diameter was 1.28 μm. The data acquisition time was 10 s. The Raman spectra were acquired in the wavenumber range of 400−1700 cm^{-1} with a resolution of 1.5 cm^{-1}. The concentration of the analytes (CV, R6G) used in all experiments was 1 μM.

The Raman mapping experiments presented in Figures 3 and 4 were conducted over an area of 30 × 30 μm^2. Each mapping was composed of a total of 625 measurements. The step length was 1.2 μm. The data acquisition time was 0.5 s. Large-scale Raman mapping measurements over a 1 × 1 mm^2 area were also employed, as shown in Figure S7. The step size was 40 μm. The objective lens magnification was 5× (0.12 NA, Leica). The data acquisition time was 0.5 s. The laser spot diameter was 8 μm. The laser spot area where the laser irradiates the sample can be approximately calculated by $(0.61\lambda/NA)^2 \times \pi$, where λ is the wavelength of the incident light. The laser spot areas in Raman mapping of a 30 × 30 μm^2 or 1 × 1 mm^2 area were found to be $\pi \times 0.639^2 = 1.28$ μm^2 or $\pi \times 4^2 = 50$ μm^2, respectively.

Calculation of the Number of Adsorbed R6G Molecules per AuNP and in the Probed Area. The number of adsorbed R6G molecules per AuNP was calculated by measuring the fluorescence intensity of R6G. Two hundred microliters of R6G solution (1 μM) was dropped onto RS-ATA for an arbitrary time (5−3600 s), 100 μL of R6G solution was taken, and the fluorescence intensity was measured using a spectrofluorometer (F-4500, Hitachi), as shown in Figure S8a. The number of adsorbed R6G molecules on the AuNPs on RS-ATA was calculated using a calibration curve (Figure S8c) prepared using R6G solutions of various concentrations. Finally, the number of R6G molecules adsorbed per AuNP (Figure S8b) was calculated from the adsorption number of R6G on d-ATA, $A_{d\text{-}ATA}$, and the FP nanocavity (TiO_2/Au film), A_{cavity}, the spot size area of the R6G solution on the RS-ATA substrate $S_{substrate}$ (8-mm-diameter circle), the surface coverage of AuNPs, C_{AuNP}, and the area of the circle at the center of AuNP, S_{AuNP}, according to eq 7.

$$\begin{aligned}&\text{R6G molecule per AuNP}\\ &= \frac{\text{total adsorption number of R6}G\text{ on AuNPs}}{\text{total number of AuNPs on d-ATA}}\\ &= \frac{A_{d\text{-}ATA} - A_{cavity}}{S_{substrate} \times C_{AuNP}} \times S_{AuNP}\end{aligned} \tag{7}$$

The laser spot radius was 0.64 μm. The total numbers of R6G molecules in the case of 0.6 molecules/AuNP and AuNPs in the probed area were found to be 3200 (5.3×10^{-21} mol) and 5320, respectively.

Simulations. FDTD simulations were performed to elucidate the near-field intensity of d-ATA using a commercial package (Lumerical, Inc.). The complex refractive indices of AuNPs, TiO_2, and Ti were adopted from the experimental data of Ciesielski et al.,[36] DeVore,[37] and Palik,[38] respectively. Circularly polarized light was used to produce an unbiased amplitude of the electric field in the plane perpendicular to the direction of light propagation. The structure unit cell was simulated with periodic boundary conditions along the x- and y-axes and a perfectly matched layer along the electromagnetic wave propagation direction (z-axis). The simulation region was chosen to be the same as that for one array unit. The mesh sizes of the simulations originating from Figures S4 and S5 were 0.2 and 0.5 nm, respectively.

ASSOCIATED CONTENT

Supporting Information

The Supporting Information is available free of charge at https://pubs.acs.org/doi/10.1021/acsnano.3c10959.

Absorption spectra of the AuNP colloidal solutions, SEM images of d-ATA after ozone cleaning, Voronoi diagram of d-AuNP, absorption spectra of d-ATA and d-AT structures with various TiO_2 thicknesses, dispersion curve of hybrid modes in the d-ATA structures, models for FDTD simulations, integrated near-field intensities for d-AT and d-ATA, cross-sectional near-field distribution on RS-AT and RS-ATA, Raman mapping images over a 1 × 1 mm^2 area of CV on d-ATA, fluorescence spectra of R6G solution and the collected R6G solution from the substrates, number of R6G molecules adsorbed on AuNPs for RS-ATA, absorption spectra of IS-AT and IS-ATA substrates decorated with different numbers of adsorbed R6G molecules per AuNP, Raman spectra for different numbers of adsorbed R6G molecules per AuNP on d-AT and d-ATA, Raman mapping for different numbers of adsorbed R6G molecules per AuNP on d-AT and d-ATA, and assignment of SERS signals for CV and R6G (PDF)

AUTHOR INFORMATION

Corresponding Author

Hiroaki Misawa − *Research Institute for Electronic Science, Hokkaido University, Sapporo 001-0021, Japan; Research Institute for Interdisciplinary Science, Okayama University, Okayama 700-8530, Japan; Center for Emergent Functional Matter Science, National Yang Ming Chiao Tung University, Hsinchu 30010, Taiwan;* orcid.org/0000-0003-1070-387X; Email: misawa@es.hokudai.ac.jp

Authors

Yoshiki Suganami − *Research Institute for Electronic Science, Hokkaido University, Sapporo 001-0021, Japan*

Tomoya Oshikiri − *Research Institute for Electronic Science, Hokkaido University, Sapporo 001-0021, Japan; Institute of Multidisciplinary Research, Tohoku University, Sendai 980-8577, Japan;* orcid.org/0000-0002-1268-0256

Hideyuki Mitomo − *Research Institute for Electronic Science, Hokkaido University, Sapporo 001-0021, Japan; Institute of Multidisciplinary Research, Tohoku University, Sendai 980-8577, Japan;* orcid.org/0000-0002-6748-7816

Keiji Sasaki − *Research Institute for Electronic Science, Hokkaido University, Sapporo 001-0021, Japan;* orcid.org/0000-0003-2340-9477

Yen-En Liu − *Research Institute for Electronic Science, Hokkaido University, Sapporo 001-0021, Japan*

Xu Shi − *Creative Research Institution, Hokkaido University, Sapporo 001-0021, Japan;* orcid.org/0000-0002-6353-5470

Yasutaka Matsuo − *Research Institute for Electronic Science, Hokkaido University, Sapporo 001-0021, Japan;* orcid.org/0000-0002-5071-0284

Kuniharu Ijiro − *Research Institute for Electronic Science, Hokkaido University, Sapporo 001-0021, Japan*

Complete contact information is available at: https://pubs.acs.org/10.1021/acsnano.3c10959

https://doi.org/10.1021/acsnano.3c10959
ACS Nano 2024, 18, 4993−5002

Author Contributions

Y. Suganami conducted all experiments and wrote the manuscript. H. Misawa, K. Sasaki, and K. Ijiro supervised the project and designed the research. H. Misawa, Y. Suganami, T. Oshikiri, H. Mitomo, X. Shi, Y. Matsuo, and K. Ijiro participated in discussions about sample preparation conditions. H. Misawa, K. Sasaki, and Y.-E. Liu contributed to the theoretical understanding of the mechanism of SERS under quantum coherence. K. Sasaki performed the theoretical model construction of quantum coherence. All authors reviewed and revised the manuscript, participated in the scientific discussions, and gave approval to the final version of the manuscript.

Notes

The authors declare no competing financial interest.

ACKNOWLEDGMENTS

We are grateful to Chie Takeuchi at Hokkaido University for preparing the d-AuNPs monolayer. We acknowledge financial support from The Japan Society for the Promotion of Science (JSPS) KAKENHI Grant Numbers JP23H05464, JP23H01916, JP22K19003, JP22H05136, JP22H05131 (a Grant-in-Aid for Transformative Research Areas "Evolution of Chiral Materials Science using Helical Light Fields"), JP21H04657, JP21H01736, and JP18H05205, Project JPNP20004 (the New Energy and Industrial Technology Development Organization (NEDO)), and "Crossover Alliance to Create the Future with People, Intelligence and Materials" and Advanced Research Infrastructure for Materials and Nanotechnology (ARIM) Japan from the Ministry of Education, Culture, Sports, Science and Technology (MEXT).

ABBREVIATIONS

SERS, surface-enhanced Raman scattering; d-AuNPs, densely packed gold nanoparticles; TiO_2, titanium dioxide; d-ATA, d-AuNPs/TiO_2/Au film; LSPR, localized surface plasmon resonances; CV, crystal violet; R6G, rhodamine 6G; FP nanocavity, Fabry−Pérot nanocavity; AuNDs, gold nanodisks; FDTD simulations, finite difference time domain simulations; d-AT, d-AuNPs/TiO_2; IS-AUNPs, irregular spherical AuNPs; RS-AuNPs, regular spherical AuNPs; DDT, 1-dodecanethiol; AuNP@DDT, DDT-modified AuNP; IS-ATA, d-ATA using IS-AuNPs; RS-ATA, d-ATA using RS-AuNPs; IS-AT, d-AT using IS-AuNPs; RS-ATA, d-ATA using RS-AuNPs

REFERENCES

(1) Fleischmann, M.; Hendra, P. J.; McQuillan, A. J. Raman Spectra of Pyridine Adsorbed at a Silver Electrode. *Chem. Phys. Lett.* **1974**, *26*, 163−166.

(2) Zong, C.; Xu, M.; Xu, L. J.; Wei, T.; Ma, X.; Zheng, X. S.; Hu, R.; Ren, B. Surface-Enhanced Raman Spectroscopy for Bioanalysis: Reliability and Challenges. *Chem. Rev.* **2018**, *118*, 4946−4980.

(3) Itoh, T.; Procházka, M.; Dong, Z. C.; Ji, W.; Yamamoto, Y. S.; Zhang, Y.; Ozaki, Y. Toward a New Era of SERS and TERS at the Nanometer Scale: From Fundamentals to Innovative Applications. *Chem. Rev.* **2023**, *123*, 1552−1634.

(4) Langer, J.; Jimenez de Aberasturi, D.; Aizpurua, J.; Alvarez-Puebla, R. A.; Auguié, B.; Baumberg, J. J.; Bazan, G. C.; Bell, S. E. J.; Boisen, A.; Brolo, A. G.; Choo, J.; Cialla-May, D.; Deckert, V.; Fabris, L.; Faulds, K.; García de Abajo, F. J.; Goodacre, R.; Graham, D.; Haes, A. J.; Haynes, C. L.; et al. Present and Future of Surface-Enhanced Raman Scattering. *ACS Nano* **2020**, *14*, 28−117.

(5) Lane, L. A.; Qian, X.; Nie, S. SERS Nanoparticles in Medicine: From Label-Free Detection to Spectroscopic Tagging. *Chem. Rev.* **2015**, *115*, 10489−10529.

(6) Yokota, Y.; Ueno, K.; Misawa, H. Essential Nanogap Effects on Surface-Enhanced Raman Scattering Signals from Closely Spaced Gold Nanoparticles. *Chem. Commun.* **2011**, *47*, 3505−3507.

(7) Borah, R.; Verbruggen, S. W. Coupled Plasmon Modes in 2D Gold Nanoparticle Clusters and Their Effect on Local Temperature Control. *J. Phys. Chem. C* **2019**, *123*, 30594−30603.

(8) Yang, Y.; Gu, C.; Li, J. Sub-5 Nm Metal Nanogaps: Physical Properties, Fabrication Methods, and Device Applications. *Small* **2019**, *15*, 1970030.

(9) Jaculbia, R. B.; Imada, H.; Miwa, K.; Iwasa, T.; Takenaka, M.; Yang, B.; Kazuma, E.; Hayazawa, N.; Taketsugu, T.; Kim, Y. Single-Molecule Resonance Raman Effect in a Plasmonic Nanocavity. *Nat. Nanotechnol.* **2020**, *15*, 105−110.

(10) Schmidt, M. M.; Farley, E. A.; Engevik, M. A.; Adelsman, T. N.; Tuckmantel Bido, A.; Lemke, N. D.; Brolo, A. G.; Lindquist, N. C. High-Speed Spectral Characterization of Single-Molecule SERS Fluctuations. *ACS Nano* **2023**, *17*, 6675−6686.

(11) Niu, R.; Gao, F.; Wang, D.; Zhu, D.; Su, S.; Chen, S.; Yuwen, L.; Fan, C.; Wang, L.; Chao, J. Pattern Recognition Directed Assembly of Plasmonic Gap Nanostructures for Single-Molecule SERS. *ACS Nano* **2022**, *16*, 14622−14631.

(12) Jiang, T.; Chen, G.; Tian, X.; Tang, S.; Zhou, J.; Feng, Y.; Chen, H. Construction of Long Narrow Gaps in Ag Nanoplates. *J. Am. Chem. Soc.* **2018**, *140*, 15560−15563.

(13) Lee, C. H.; Hankus, M. E.; Tian, L.; Pellegrino, P. M.; Singamaneni, S. Highly Sensitive Surface Enhanced Raman Scattering Substrates Based on Filter Paper Loaded with Plasmonic Nanostructures. *Anal. Chem.* **2011**, *83*, 8953−8958.

(14) Gersten, J.; Nitzan, A. Electromagnetic Theory of Enhanced Raman Scattering by Molecules Adsorbed on Rough Surfaces. *J. Chem. Phys.* **1980**, *73*, 3023−3027.

(15) Schulz, F.; Pavelka, O.; Lehmkühler, F.; Westermeier, F.; Okamura, Y.; Mueller, N. S.; Reich, S.; Lange, H. Structural Order in Plasmonic Superlattices. *Nat. Commun.* **2020**, *11*, 3821.

(16) Wang, K.; Ling, H.; Bao, Y.; Yang, M.; Yang, Y.; Hussain, M.; Wang, H.; Zhang, L.; Xie, L.; Yi, M.; Huang, W.; Xie, X.; Zhu, J. A Centimeter-Scale Inorganic Nanoparticle Superlattice Monolayer with Non-Close-Packing and Its High Performance in Memory Devices. *Adv. Mater.* **2018**, *30*, 1800595.

(17) Matricardi, C.; Hanske, C.; Garcia-Pomar, J. L.; Langer, J.; Mihi, A.; Liz-Marzán, L. M. Gold Nanoparticle Plasmonic Superlattices as Surface-Enhanced Raman Spectroscopy Substrates. *ACS Nano* **2018**, *12*, 8531−8539.

(18) Wang, H.; Yao, L.; Mao, X.; Wang, K.; Zhu, L.; Zhu, J. Gold Nanoparticle Superlattice Monolayer with Tunable Interparticle Gap for Surface-Enhanced Raman Spectroscopy. *Nanoscale* **2019**, *11*, 13917−13923.

(19) Mueller, N. S.; Pfitzner, E.; Okamura, Y.; Gordeev, G.; Kusch, P.; Lange, H.; Heberle, J.; Schulz, F.; Reich, S. Surface-Enhanced Raman Scattering and Surface-Enhanced Infrared Absorption by Plasmon Polaritons in Three-Dimensional Nanoparticle Supercrystals. *ACS Nano* **2021**, *15*, 5523−5533.

(20) Arul, R.; Grys, D.-B.; Chikkaraddy, R.; Mueller, N. S.; Xomalis, A.; Miele, E.; Euser, T. G.; Baumberg, J. J. Giant Mid-IR Resonant Coupling to Molecular Vibrations in Sub-Nm Gaps of Plasmonic Multilayer Metafilms. *Light Sci. Appl.* **2022**, *11*, 281.

(21) Cecchini, M. P.; Turek, V. A.; Paget, J.; Kornyshev, A. A.; Edel, J. B. Self-Assembled Nanoparticle Arrays for Multiphase Trace Analyte Detection. *Nat. Mater.* **2013**, *12*, 165−171.

(22) Mitomo, H.; Horie, K.; Matsuo, Y.; Niikura, K.; Tani, T.; Naya, M.; Ijiro, K. Active Gap SERS for the Sensitive Detection of Biomacromolecules with Plasmonic Nanostructures on Hydrogels. *Adv. Opt. Mater.* **2016**, *4*, 259−263.

(23) Nam, J. M.; Oh, J. W.; Lee, H.; Suh, Y. D. Plasmonic Nanogap-Enhanced Raman Scattering with Nanoparticles. *Acc. Chem. Res.* **2016**, *49*, 2746−2755.

https://doi.org/10.1021/acsnano.3c10959
ACS Nano 2024, 18, 4993−5002

(24) Arbuz, A.; Sultangaziyev, A.; Rapikov, A.; Kunushpayeva, Z.; Bukasov, R. How Gap Distance between Gold Nanoparticles in Dimers and Trimers on Metallic and Non-Metallic SERS Substrates Can Impact Signal Enhancement. *Nanoscale Adv.* **2021**, *4*, 268−280.
(25) Chen, H. Y.; Lin, M. H.; Wang, C. Y.; Chang, Y. M.; Gwo, S. Large-Scale Hot Spot Engineering for Quantitative SERS at the Single-Molecule Scale. *J. Am. Chem. Soc.* **2015**, *137*, 13698−13705.
(26) Han, Y.; Han, Y.; He, Q.; Liu, H.; Zhang, Y.; Han, L. Ultrasensitive and Reliable SERS Chip Based on Facile Assembly of AgNPs on Porous LIG to Enhance the Local Electromagnetic Field. *J. Phys. Chem. C* **2023**, *127*, 4195−4202.
(27) Zang, X.; Shi, X.; Oshikiri, T.; Ueno, K.; Sunaba, Y.; Sasaki, K.; Misawa, H. Highly Sensitive and Spatially Homogeneous Surface-Enhanced Raman Scattering Substrate under Plasmon-Nanocavity Coupling. *J. Phys. Chem. C* **2021**, *125*, 19880−19886.
(28) Liu, Y. E.; Shi, X.; Yokoyama, T.; Inoue, S.; Sunaba, Y.; Oshikiri, T.; Sun, Q.; Tamura, M.; Ishihara, H.; Sasaki, K.; Misawa, H. Quantum-Coherence-Enhanced Hot-Electron Injection under Modal Strong Coupling. *ACS Nano* **2023**, *17*, 8315−8323.
(29) Tsutsui, G.; Huang, S.; Sakaue, H.; Shingubara, S.; Takahagi, T. Well-Size-Controlled Colloidal Gold Nanoparticles Dispersed in Organic Solvents. *Jpn. J. Appl. Phys.* **2001**, *40*, 346−349.
(30) Mitomo, H.; Takeuchi, C.; Sugiyama, R.; Tamada, K.; Ijiro, K. Thermo-Responsive Silver Nanocube Assembled Films. *Bull. Chem. Soc. Jpn.* **2022**, *95*, 771−773.
(31) Langmuir, I.; Schaefer, V. J. Activities of Urease and Pepsin Monolayers. *J. Am. Chem. Soc.* **1938**, *60*, 1351−1360.
(32) Shi, X.; Ueno, K.; Oshikiri, T.; Sun, Q.; Sasaki, K.; Misawa, H. Enhanced Water Splitting under Modal Strong Coupling Conditions. *Nat. Nanotechnol.* **2018**, *13*, 953−958.
(33) Gao, W.; Li, X.; Bamba, M.; Kono, J. Ultrastrong Coupling through Exceptional Points in Carbon Nanotube Microcavity Exciton-Polaritons. *Nat. Photonics* **2018**, *12*, 362−368.
(34) Sergiienko, S.; Moor, K.; Gudun, K.; Yelemessova, Z.; Bukasov, R. Nanoparticle-Nanoparticle vs. Nanoparticle-Substrate Hot Spot Contributions to the SERS Signal: Studying Raman Labelled Monomers, Dimers and Trimers. *Phys. Chem. Chem. Phys.* **2017**, *19*, 4478−4487.
(35) Itoh, T.; Hashimoto, K.; Ikehata, A.; Ozaki, Y. Changes in Excitation Profiles of Surface-Enhanced Resonance Raman Scattering Induced by Changes in Surface Plasmon Resonance of Single Ag Nano-Aggregates. *Chem. Phys. Lett.* **2004**, *389*, 225−229.
(36) Ciesielski, A.; Skowronski, L.; Trzcinski, M.; Górecka, E.; Trautman, P.; Szoplik, T. Evidence of Germanium Segregation in Gold Thin Films. *Surf. Sci.* **2018**, *674*, 73−78.
(37) DeVore, J. R. Refractive Indices of Rutile and Sphalerite. *J. Opt. Soc. Am.* **1951**, *41*, 416−419.
(38) Palik, E. D. *Handbook of Optical Constants of Solids*; Academic Press: San Diego, 1998.

https://doi.org/10.1021/acsnano.3c10959
ACS Nano 2024, 18, 4993−5002